



Effect of Cooling Rate on Pitting Corrosion Behavior of 904L Austenitic Stainless Steel in a Simulated Flue Gas Desulfurization Solution

Miaomiao Li¹ · Dening Zou¹ · Yunong Li¹ · Libo Tong¹

Received: 8 March 2022 / Accepted: 29 May 2022 / Published online: 6 August 2022
© The Author(s) under exclusive licence to The Korean Institute of Metals and Materials 2022

Abstract

904L super austenitic stainless steel is prone to harmful secondary phase precipitation, which reduces corrosion resistance. The cooling rate during the solidification of steel is one of the critical factors affecting the precipitation of brittle phases in stainless steel metals. In this paper, the effect of the cooling rates (6, 50, 100, 500, and 1000 °C min⁻¹) on the initial corrosion behavior of 904L steel in a simulated flue gas desulfurization (FGD) solution was studied by electrochemical measurements and microscopic morphology observation. The results show that as the cooling rates increases, the primary solidification temperature and the secondary dendrite arm spacing decrease. The precipitated phase in the steel is a σ -phase mainly distributed interdendrites and forms zones of chromium and molybdenum depletion, reducing pitting resistance. With the increase in the cooling rate, the corrosion resistance increases first and then decreases, and reaches the maximum at 100 °C min⁻¹. At the same time, different cooling rates result in different contents of Cr and Mo in σ phase. At 100 °C min⁻¹, the concentration gradient of Cr and Mo near the interdendrites is the lowest compared with other cooling rates, which inhibits the growth rate of the σ phase nuclei and produces a more uniform microstructure. Corrosion test results show that pitting corrosion is sensitive to the increase in the contents of Cr and Mo in the σ phase. The higher the content of Cr and Mo in the σ phase, the more serious the depletion of Cr and Mo near the interdendrites, and the worse the corrosion resistance.

Keywords 904L super austenitic stainless steel · Different cooling rates · σ phase · Pitting corrosion · Flue gas desulfurization solution

1 Introduction

Since the presence of a certain amount of acidic components (mainly SO₃) in the flue gas desulfurization (FGD) of thermal power plants, equipment parts are susceptible to severe corrosion by acidic condensates such as sulfuric acid, chloride, fluoride and nitrate [1–5]. 904L super austenitic stainless steel (904L SASS) has higher Cr, Mo, and Ni contents compared with AISI 304L and 316L [6–8]. Due to the high alloy content, the pitting resistance equivalent number (PREN = [wt%Cr] + 3.3 [wt%Mo] + 30 [wt%N]) of 904L SASS (32.5–39.5) is much higher than that of ASS 316L (22.6–27.9) [9, 10]. Therefore, in an acidic environment, 904L SASS has better intergranular, pitting, crevice, and high-stress corrosion resistance than traditional stainless

steel [11–13], which is widely used in the FGD field with high corrosion resistance in the poor working conditions.

However, many factors such as chemical composition, microstructure, impurities, inclusions, precipitates, grain size, and structure will affect the performance of 904L SASS [14–17]. In the solidification process, the high content of Cr and Mo causes 904L SASS to be unstable at high temperatures, forming a heterogeneous microstructure consisting of intermetallic compounds and dendritic austenite [18, 19]. At the same time, element segregation and secondary phase precipitation seriously deteriorate the microstructure and composition uniformity of castings. It is easy for the material to form crack sources near these precipitated phases during service. Accordingly, the mechanical properties and corrosion resistance of the material will decrease [19].

Studies have shown that one of the key factors for obtaining high austenite content without harmful phases is the cooling rate, and a slow cooling rate will cause the precipitation of brittle intermetallic phases (σ phase or χ phase) [20–22]. Chen et al. [23] studied the effect of cooling rate on the phase

✉ Dening Zou
zoudening@sina.com

¹ School of Metallurgical Engineering, Xi'an University of Architecture and Technology, Xi'an 710055, China

content of duplex stainless steel, thereby affecting its pitting resistance. Han et al. [24] found that high cooling rate could reduce the width of chromium depletion region, thereby improving the corrosion resistance of 5Cr15MoV steel. In the study of corrosion resistance of 904L SASS, Wang et al. [25] studied that the existence of σ phase at the grain boundary causes the chromium—depleted zones, resulting in intergranular corrosion of metals. Barbosa et al. [9] also found that the existence of the second phase (chromium carbide, chi phase and σ phase) in 904L SASS had a strongly influence on the corrosion resistance. Unfortunately, so far, no in-depth studies have been conducted on the effect of the cooling rate during solidification on the microstructure evolution, precipitation behavior, and corrosion resistance of 904L SASS.

In this paper, high-temperature confocal laser scanning microscopy (HT-CLSM) is used to dynamically observe the solidification process of 904L SASS under different cooling rates (6, 50, 100, 500, and 1000 °C min⁻¹). The effects of different cooling rates on the solidification process and microstructure are studied by scanning electron microscopy (SEM), energy dispersive spectrometer (EDS), and backscattered diffraction (BSD). With the simulated FGD environment as the corrosion medium, the pitting corrosion behavior at different cooling rates is studied with electrochemical technology. The relationship between the solidification structure at different cooling rates and the pitting corrosion behavior is clarified by observing the surface morphology and elemental characterization after electrochemical treatment at different cooling rates, which reveals the corrosion mechanism of 904L SASS.

2 Experimental Materials and Methods

2.1 Material Preparation

In the present study, the 904L SASS ingot is produced by Shanxi Titanium Steel Stainless Steel Co., Ltd. The chemical constituents of test steel are shown in Table 1.

2.2 HT-CLSM Experiments

To observe the surface microstructure evolution of 904L SASS during solidification, the sample of ϕ 7.8 × h 3 mm was cut, cleaned, and polished. Chemical etching is not required in HT-CLSM research. The polished samples were placed in the Al₂O₃ crucible on the sample holder, and then rinsed with high-purity argon to exhaust the furnace chamber gas. Throughout the entire experiment, argon flushing remained unchanged. Controlling the atmosphere in the furnace was a

decisive factor for the success of the research, as the occurrence of the surface oxidation phenomenon has various negative effects. The actual test was carried out after the residual oxygen content reached < 1 ppm in the furnace chamber. To this end, the time–temperature cycle required in the corresponding software was defined and started. The temperature control standard of the infrared heating furnace was carried out by a Type-S thermocouple installed on the lower side of the sample holder. However, the result of this arrangement is that there is a certain temperature difference between the controlled furnace temperature and the sample surface.

For the continuous heating and cooling experiment (Fig. 1), the sample was slowly heated to 200 °C at 50 °C min⁻¹, which was then heated to 1440 °C to melt the sample completely at 100 °C min⁻¹. Subsequently, the samples were kept at 1440 °C for 3 min, cooled to 1200 °C at the cooling rates of 6, 50, 100, 500, and 1000 °C min⁻¹, and then cooled to room temperature at 1200 °C min⁻¹. The sample surface was evaluated immediately after the HT-CLSM experiment. These samples then underwent grinding and polishing so that an area of about 100 μ m below the original surface can be studied.

2.3 Characterization

The samples were polished and mechanically etched for 60 s (10% oxalic acid, 6 V voltage, 0.25 A/cm²). Then the sample was washed with distilled water and alcohol and dried. The casting dendrite and optical microstructure of homogeneous samples were observed by the Olympus—GX51 optical

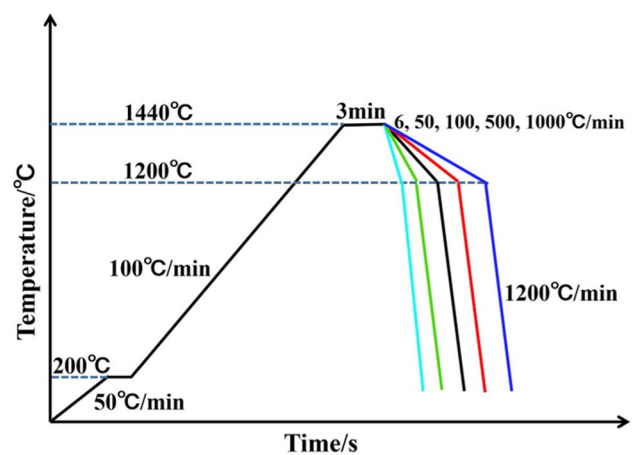


Fig. 1 The preparation process of 904L SASS at different cooling rates

Table 1 The chemical constituents of 904L SASS (wt%)

C	Cr	Ni	Mn	Si	P	Mo	N	Cu	S	Fe
0.009	20.100	25.590	1.500	0.420	0.021	4.490	0.060	1.300	0.003	Bal

microscope. The ImagePro software was used to measure the secondary dendrite arm spacing at spacing at different cooling rates. Electropolishing (10% perchloric acid + 90% alcohol, 30 V, 0.25 A/cm², 60 s) samples were dried for 1 h in a vacuum drying oven, and the microstructure was characterized by SEM (Gemini SEM 300). The content of each element in the target area was qualitatively analyzed by EDS.

The corrosion resistance of 904L SASS at different cooling rates was tested in the simulated FGD environment solution (11.4 wt% H₂SO₄ + 1.2 wt% HCl + 1 wt% FeCl₃ + 1 wt% CuCl₂) at room temperature by an electrochemical workstation (Gamry Reference 600+). The working system is a three-electrode battery, in which the platinum plate is the counter electrode, the saturated calomel electrode is the reference electrode, and the sample with an exposed area of 0.5 cm² is the working electrode. The measurement time of the open circuit potential is 3600 s. The test frequency of electrochemical impedance spectroscopy is 10⁻²~10⁶ Hz. The test results were fitted and analyzed by ZSimpWin3.10 software. Based on open circuit potential, the polarization curve was tested from -1 to 1.5 V, and the scanning rate was 5 mV/s. The corrosion parameters were obtained by Tafel extrapolation.

The thickness of the passive film can be calculated by the capacitance parameters obtained from the above electrochemical impedance spectroscopy. The data of the constant phase angle component *CPE* (Ω⁻¹Sⁿcm⁻²) is obtained by the equivalent circuit fitting, and the pure capacitance parameter *C* (F cm⁻²) is used to calculate the passive film thickness. Therefore, the value of *C* is calculated by formula (1) [26], and then the passive film thickness *d* is obtained by formula (2) [27].

$$C = \frac{1}{2\pi f_{\theta_{max}} |Z|_{\theta_{max}}}, \quad (1)$$

$$d = \frac{\epsilon \epsilon_0 A}{C}, \quad (2)$$

where $f_{\theta_{max}}$ is the frequency corresponding to the maximum phase angle, the unit is HZ; $|Z|_{\theta_{max}}$ is the impedance modulus corresponding to the maximum phase angle, the unit is Ω cm⁻²; ϵ is the dielectric constant of the passive film (usually 15.6) [28]; ϵ_0 is the vacuum dielectric constant (8.85 × 10⁻¹² F m⁻¹); *A* is the effective area of the passive film; *C* is the capacitance of the passive film; and *d* is the thickness of the passive film.

3 Results

3.1 Influence of Different Cooling Rates on Microstructure Evolution

Figure 2 shows the HT-CLSM images of microstructure evolution during solidification at a series of different cooling rates. Figure 2a–d exhibits the solidification evolution at 6 °C min⁻¹. In the early stage of solidification, the austenite (γ) phase nucleates from the liquid. With the continuous decrease in temperature, the nucleus grows, thickens, and begins to grow in all directions. As the nucleus continues to grow, the unit cell exhibits a dendritic morphology and is emitted from the dendrite stem by many secondary dendrites. When the temperature drops below the solid line, some residual liquids still exist in the interdendritic region (Fig. 2c). It is believed that this phenomenon should be caused by element segregation and abnormal component supercooling. Finally, the liquid phase is completely solidified, and complete dendrites can be clearly observed in Fig. 2d. Under the conditions of 50, 100, 500, and 1000 °C min⁻¹, the growth of the dendrites shows similar evolution behavior as that under the condition of 6 °C min⁻¹. By comparing the dendrite morphology at different cooling rates, it is found that the nucleation of the cell is larger and the growth trend of the main dendrite is better at a lower cooling rate. At a higher cooling rate, smaller and more nuclei could be observed, and the dendrites grow rapidly with more levels, and the secondary dendrite arms are more luxuriant. By observing the HT-CLSM field of the solidification process, the solidification temperature at different cooling rates is different, and the approximate initial temperature and the final temperature of solidification at different cooling rates can be obtained, as shown in Table 2. With the increase in the cooling rate, the approximate initial temperature and final temperature of solidification gradually decrease. During the solidification of 904L SASS, the temperature at which the γ phase begins to nucleate from the liquid decreases with the increase in the cooling rate.

Figure 3 presents the microstructure of the metal phase obtained by the 904L SASS etching surface at different cooling rates. The results show that the dendrites are gradually refined with the increase in the cooling rate, and the secondary dendrite arm spacing under different cooling rates is measured and analyzed (Fig. 3f). In fact, the size of the secondary dendrites is constantly changing during solidification. The components near the dendrite surface vary from place to place and diffuse from the high solubility region to the low solubility region, resulting in the dissolution of the fine dendrite arm and the coarsening of the coarse dendrite arm. With the increase in the cooling

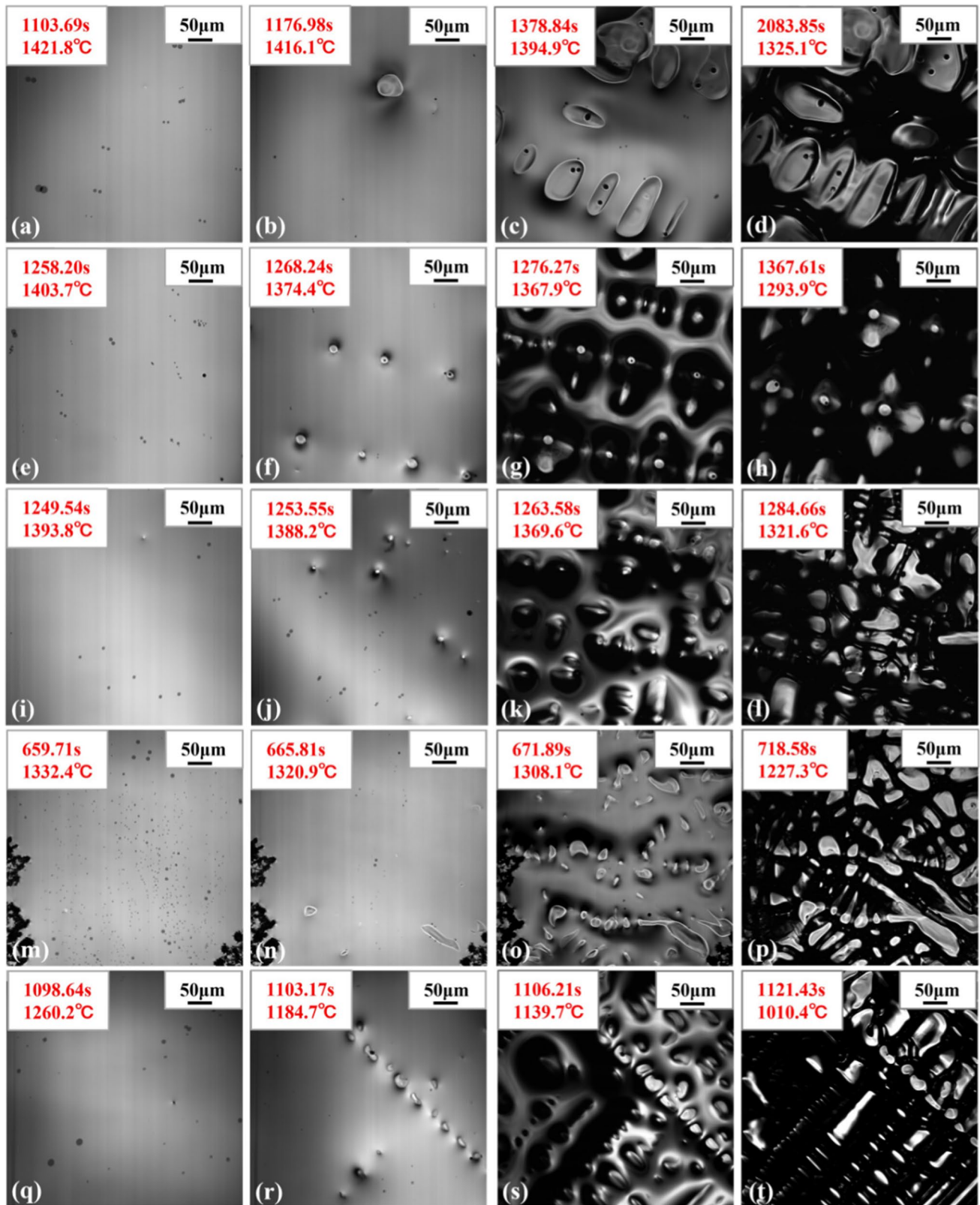


Fig. 2 The in-situ observation diagram of solidification process of 904L SASS at different cooling rates by HT-CLSM: **a–d** $6\text{ }^{\circ}\text{C min}^{-1}$, **e–h** $50\text{ }^{\circ}\text{C min}^{-1}$, **i–l** $100\text{ }^{\circ}\text{C min}^{-1}$, **m–p** $500\text{ }^{\circ}\text{C min}^{-1}$, and **q–t** $1000\text{ }^{\circ}\text{C min}^{-1}$

Table 2 Initial and final solidification temperatures at different cooling rates

Cooling rates ($^{\circ}\text{C min}^{-1}$)	Initial solidification temperature ($^{\circ}\text{C}$)	Final solidification temperature ($^{\circ}\text{C}$)
6	1421.8	1325.1
50	1403.7	1293.9
100	1393.8	1321.6
500	1332.4	1227.3
1000	1260.2	1010.4

rate, the elements do not have enough time to diffuse, so the secondary dendrite arms are refined and secondary dendrite arm spacing gradually decreases.

The backscattering diffraction observation of the HT-CLSM samples obtained in various cooling rates is presented in Fig. 4. Regardless of the cooling rate, the microstructure is composed of a complete austenite dendrite structure and precipitates are generated during solidification. The precipitation-formed interdendrites (white area) are regularly island-like, as shown in Fig. 4a–e. Generally, elements with relatively low solubility in the initial solid phase are segregated between dendrites during solidification. Therefore, it is easy for the second phase to generate in the interdendritic region. The content of the elements presented in Fig. 4k–m and Table 3 shows the EDS analysis of the matrix (spectra 4) and precipitates (spectra 1, 2, and 3) at

three cooling rates. The main components of the austenite dendrite are iron, chromium, nickel, and molybdenum. Spectra 4 shows that the content of each element in the test steel matrix is consistent with the austenite dendrite. The precipitated phase (spectra 1, 2, and 3) shows that the contents of Mo and Cr are much higher than that of the austenite matrix. The crystal structure of the precipitated phase is consistent with the composition characteristics of Mo and Cr in the σ precipitates in austenite. Therefore, it can confirm that the precipitate is the σ phase precipitated in the interdendrites [29, 30].

According to some studies [21, 31, 32], the formation of the σ phase is related to high temperature, cooling rate, Fe, Cr, Mo, and other large-scale atomic diffusion rates. This led to the emergence of depleted and enriched areas of these elements. With the occurrence of the solidification process (Fig. 2), the austenite dendrites are firstly solidified; Fe, Cr, Mo, and other larger-sized atoms are excluded from the residual liquid phase between dendrites; and, finally, the σ phase is formed in the interdendrites. By analyzing the σ phase microstructure changes at different cooling rates (Fig. 4f–g), it can be determined that when the cooling rate is $6^{\circ}\text{C min}^{-1}$, due to sufficient time for the σ phase to nucleate and grow from the matrix, a large number of reticular precipitates are observed in the interdendrites. With the increase in the cooling rate, the size of the σ phase decreases. When the cooling rate is $100^{\circ}\text{C min}^{-1}$, the precipitated phase presents small lamellar. With the

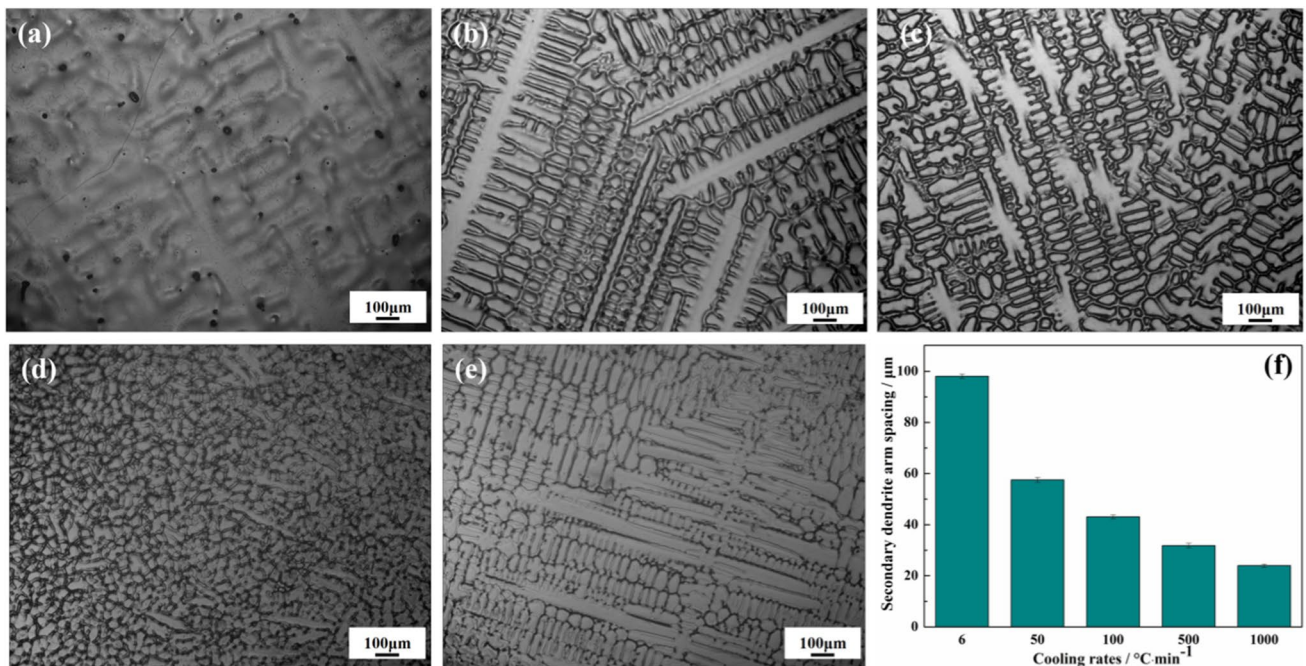


Fig. 3 The microstructures of 904L SASS at different cooling rates: **a** $6^{\circ}\text{C min}^{-1}$, **b** $50^{\circ}\text{C min}^{-1}$, **c** $100^{\circ}\text{C min}^{-1}$, **d** $500^{\circ}\text{C min}^{-1}$, **e** $1000^{\circ}\text{C min}^{-1}$, and **f** secondary dendrite arm spacing

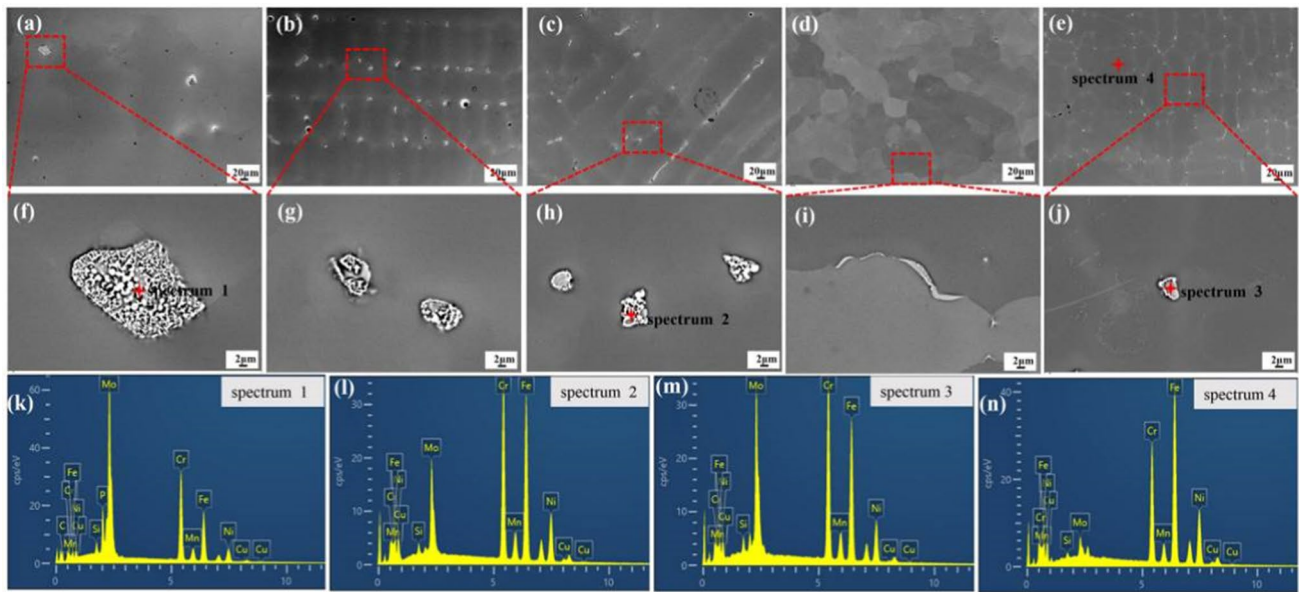


Fig. 4 The BSD microstructures of the HT-CLSM samples obtained in various cooling rates: **a, f** $6\text{ }^{\circ}\text{C min}^{-1}$, **b, g** $50\text{ }^{\circ}\text{C min}^{-1}$, **c, h** $100\text{ }^{\circ}\text{C min}^{-1}$, **d, i** $500\text{ }^{\circ}\text{C min}^{-1}$, and **e, j** $1000\text{ }^{\circ}\text{C min}^{-1}$. The EDS spectra of **k** $6\text{ }^{\circ}\text{C min}^{-1}$, **l** $100\text{ }^{\circ}\text{C min}^{-1}$, **m** $1000\text{ }^{\circ}\text{C min}^{-1}$, and **n** matrix

Table 3 The EDS results of the matrix (spectra 4) and precipitates (spectra 1, 2, and 3)

Element (wt%)	Si	Cr	Mn	Fe	Ni	Cu	Mo
Spectrum 1	0.80	30.66	1.06	20.97	9.61	0.60	36.29
Spectrum 2	0.73	26.44	1.70	37.93	17.92	1.34	13.93
Spectrum 3	1.02	27.80	1.57	31.50	13.88	0.52	23.71
Spectrum 4	0.46	20.60	1.31	49.13	23.31	1.28	3.91

increase in the cooling rate, the width of the precipitation layer decreases and develops into a continuous shape. When the cooling rate is $1000\text{ }^{\circ}\text{C min}^{-1}$, the precipitates appear as uneven flakes, and the edge is bright white and gray in the middle. This is because the increase in the cooling rate shortens the σ phase precipitation time, while the large-size σ phase does not have enough time to precipitate, resulting in dispersed and small-size nucleation in the microstructure.

The elements of Cr and Mo are segregated from the dendritic nucleus to the boundary, which related to the low solubility of Cr and Mo in the γ phase during the solidification process of the A mode [33]. During the solidification of the 904L SASS, the precipitation of the σ phase can be directly produced by the retained liquid remaining in the interdendrites. Therefore, the precipitation of the σ phases precipitation may be significantly affect by the composition of the segregated liquid during solidification. At the same time, the precipitate contains higher Cr and Mo than the matrix, so the precipitation may be affected by the behavior of Cr and Mo during solidification. However, the increase in the cooling rate reduces the

Table 4 The average content of Cr and Mo in the σ phase at different cooling rates

Cooling rates ($^{\circ}\text{C min}^{-1}$)	Mo (wt%)	Cr (wt%)
6	35.32	30.98
50	28.35	27.79
100	13.98	22.72
500	20.78	27.50
1000	23.71	28.13

initial solidification temperature of 904L SASS, resulting in a highly segregated liquid phase, which will affect the segregation of main elements (Cr and Mo) in σ phase to a certain extent. Table 4 shows the average content of Cr and Mo in the σ phase at different cooling rates of 904L SASS. The Cr and Mo contents in the σ phase increase and then decrease with the increase in the cooling rate, reaching the minimum value (22.72 wt% and 13.98 wt%) at $100\text{ }^{\circ}\text{C min}^{-1}$.

3.2 Effect of Cooling Rate on Electrochemical Performance

Figure 5a is the polarization curve of 904L SASS under different cooling conditions in a simulated FGD solution. For various cooling rates, the test steels exhibited significant passivation behaviour following anodic polarization and metastable pitting activity. This is due to the presence of Cr in test steel that reacts with dissolved O_2 to form a passivating (chemically inactive) layer of Cr_2O_3 and $Cr(OH)_3$, which has strong resistance to dew point corrosion. The existence of a passive film can separate the matrix alloy from the corrosion solution, which can effectively hinder the dissolution of the matrix alloy elements into the solution or the diffusion of oxygen in the solution into the matrix, so the corrosion current is small. As the potential continues to increase, the current density suddenly increases, indicating that the passive film ruptures and loses the protection of the matrix alloy, causing the stainless steel to be corroded.

Potentiostatic parameters showing corrosion potential (E_{corr}), metastable pitting potential (E_{pp}), metastable pitting current (i_{cp}), passivation potential (E_p), transpassivation potential [pitting potential (E_{tr})], and passivation range (E_{pr}) for 904L SASS are presented in Fig. 5b. Although the E_{corr} of stainless steel with different compositions is not very different, there are some differences in other electrochemical parameters, indicating that different cooling rates will have effects on the corrosion resistance of 904L SASS. The dense current transients at the beginning of passivation indicated that the passivation film formed on 904L SASS is unstable. Before the stable passivation of the test steel, the metastable pitting portion of the polarization curve follows the anodic polarization process of 904L SASS. In this portion of the polarization curve, a collapse of the passive film and repassivation events occur at potentials well below the potential

for stable pitting propagation [34–36]. The E_{pp} of 904L SASS increases first and then decreases with the increase in cooling rate. The i_{cp} of 904L SASS decreases first and then increases with the increase in the cooling rate. In previous research [5], it is known that the SO_4^{2-} ions can inhibit the occurrence of corrosion pits in the presence of Cl^- ions, hence the relatively stable passivation plots. However, some other studies indicate increased vulnerability to pitting corrosion [37, 38]. The E_{pr} shows the effect of corrosive ions adsorption on the 904L SASS. It is evident that the difference in the cooling rate affects the localized corrosion resistance of the 904L SASS. At $6\text{ }^\circ\text{C min}^{-1}$, the E_{pr} of the test steel is 0.635 V. Beyond $6\text{ }^\circ\text{C min}^{-1}$, the E_{pr} value increases and reaches a maximum of 0.846 V at $100\text{ }^\circ\text{C min}^{-1}$. As the cooling rate continues to rise, the E_{pr} of the stainless steel gradually decreases, while the critical current of the passivation density increases, the passive film stability decreases, and the corrosion resistance decreases. The results of E_{tr} of the steel at each cooling rate are compared, which still showed the result of increasing first and then decreasing. Unlike other parameters, the E_{tr} of $100\text{ }^\circ\text{C min}^{-1}$ is lower than that of $500\text{ }^\circ\text{C min}^{-1}$. Nevertheless, the decrease in pitting potential values (E_{tr}) for $100\text{ }^\circ\text{C min}^{-1}$ where net out by early onset of passivation of the steel resulting in extended passivation range. The corrosion resistance of 904L SASS is first enhanced and then weakened with the cooling rate, where the best cooling rate is $100\text{ }^\circ\text{C min}^{-1}$.

The Nyquist plot of the Electrochemical Impedance Spectroscopy test results of 904L SASS at different cooling rates is presented in Fig. 9. It can be seen from the Nyquist diagram that the stainless steel samples cooled in various cooling rates show a single semi-circular capacitive reactance arc, indicating that they all have capacitance characteristics, in other words, a passive film is formed on the electrode surface. Figure 9a shows that the size of the capacitive arc is

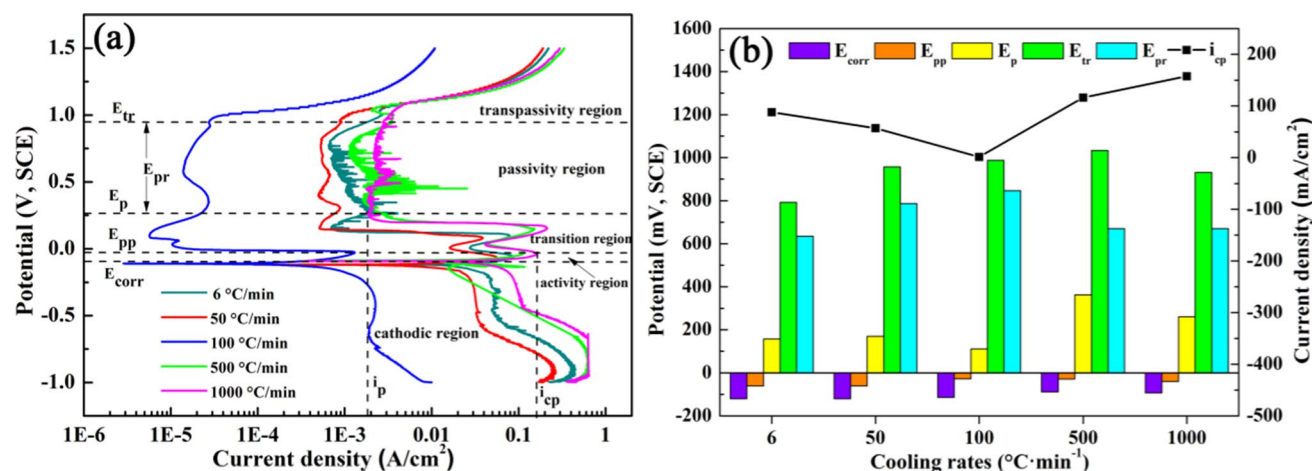


Fig. 5 a Potential polarization curves and b potentiostatic parameter change diagram of 904L SASS in various cooling rates

quite different, and the capacitive arc at $100\text{ }^{\circ}\text{C min}^{-1}$ is the largest, indicating that the corrosion resistance is the strongest compared to other cooling rates, which is consistent with the analysis results of the polarization curves.

From the $f-|Z|$ curve (Fig. 6b), the impedance values of the samples at different cooling rates have little difference in the high-frequency region, which is related to the concentration stability of the system solution. In the intermediate frequency region, $f-|Z|$ is approximately a 45° oblique line, indicating that the corrosion process is mainly controlled by mass transfer, which is mainly due to the penetration of oxygen vacancy/metal ion gap in the passive film [39]. In the low frequency stage, with the change in the cooling rate, the impedance modulus $|Z|$ is different, where $|Z|$ is maximum at $100\text{ }^{\circ}\text{C min}^{-1}$ and $|Z|$ is minimum at $6\text{ }^{\circ}\text{C min}^{-1}$. Generally, the larger the phase angle, the wider the frequency range corresponding to the peak, the better the capacitance characteristics of the passive film, and the stronger the corrosion resistance. From the phase angle curve (Fig. 6c), each cooling rate sample has only one peak in the low-frequency range, and the phase angle is the largest at $100\text{ }^{\circ}\text{C min}^{-1}$.

The above information shows that when the cooling rate is $100\text{ }^{\circ}\text{C min}^{-1}$, the resistance of the charge transfer in the stainless steel is greater, the ability to hinder metal dissolution is the strongest, and the corrosion resistance is the best.

Figure 6d is the equivalent circuit diagram for fitting, where R_s is the solution resistance, R_f is the passive film resistance, R_{ct} is the charge transfer resistance, CPE_1 is the double-layer capacitance at the interface between passive film and solution, and CPE_2 is the interface capacitance between the stainless steel substrate and passive film. By comparing the fitting data extracted from the impedance test (Table 5), it can be seen that with the increase in the cooling rate, the R_{ct} increases first and then decreases. The decrease in the R_{ct} indicates the increase in point defect density of the passive film. The R_{ct} reaches its maximum when the cooling rate is $100\text{ }^{\circ}\text{C min}^{-1}$, which demonstrate that the passive film on the surface of stainless steel under this condition is the most uniform and dense, the ability to hinder metal dissolution is the strongest, and the corrosion resistance is the strongest. On the contrary, the corrosion resistance is the worst when the cooling rate is $6\text{ }^{\circ}\text{C min}^{-1}$.

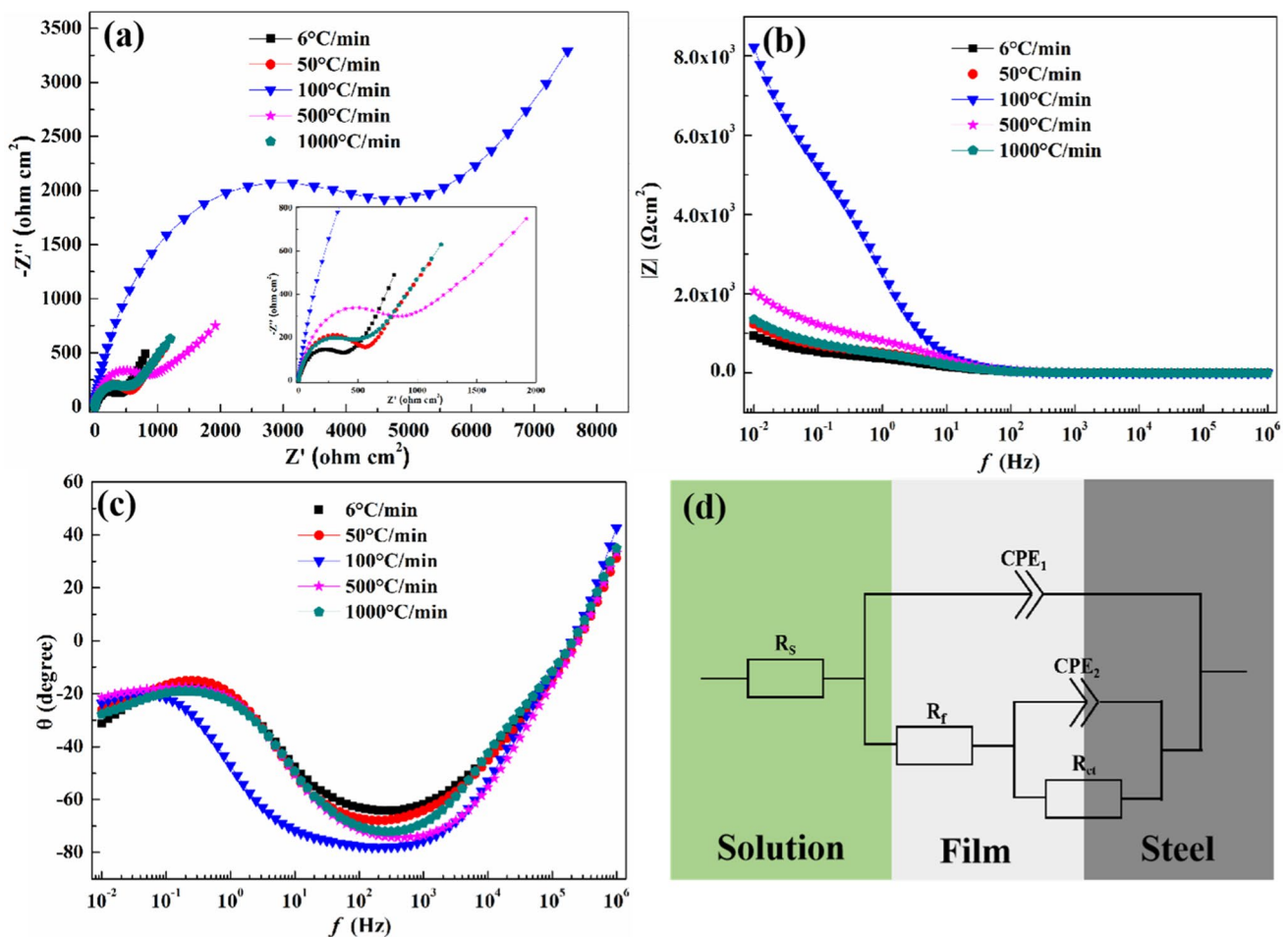
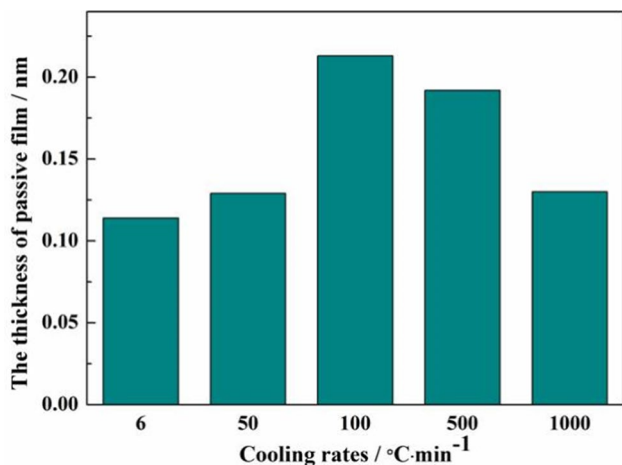


Fig. 6 **a** The Nyquist plot, **b** bode plots, **c** phase angle, and **d** equivalent circuit of 904L SASS in an FGD solution

Table 5 Electrochemical parameters fitted by EIS polt of 904L SASS in the FGD solution

Sample (°C min ⁻¹)	R_s (Ω cm ²)	CPE_1		R_f (Ω cm ²)	CPE_1		R_{ct} (Ω cm ²)
		Y_1 (Ω^{-1} cm ⁻² s ⁻ⁿ)	n_1		Y_2 (Ω^{-1} cm ⁻² s ⁻ⁿ)	n_2	
6	0.7409	1.35×10^{-4}	0.7938	571.0	5.953×10^{-3}	0.6178	3907
50	0.6039	5.45×10^{-5}	0.8683	572.5	1.584×10^{-3}	0.3089	4.31×10^{10}
100	0.7228	1.97×10^{-4}	0.7690	377.1	5.877×10^{-3}	0.4862	4.96×10^{13}
500	0.6634	5.01×10^{-5}	0.8842	337.8	4.714×10^{-4}	0.3376	1.42×10^{13}
1000	0.6957	1.05×10^{-4}	0.8432	409.7	2.979×10^{-3}	0.3949	1.98×10^{11}

**Fig. 7** The passive film thickness of 904L SASS by different cooling rates

The thickness of the passive film on the 904L SASS surface with different cooling rates can be calculated by formulas (1) and (2), where the calculation results are shown in Fig. 7. The variation law of the thickness of the passive film is consistent with that of the corresponding electrochemical corrosion. The passive film is the thickest when the cooling rate is $100 \text{ }^\circ\text{C min}^{-1}$ and the thinnest when the cooling rate is $6 \text{ }^\circ\text{C min}^{-1}$.

3.3 XPS Analysis

Figure 8 shows the detailed spectra of Fe $2p_{3/2}$, Cr $2p_{3/2}$, Mo $3d$, Ni $2p_{3/2}$ and O1s after deconvolution along with the calculated proportion of different components. Fe^{3+} compounds are the primary constituents of the oxidized Fe species (Fig. 8a). The $\text{Fe}^{2+}/\text{Fe}^{3+}$ ratio decreased from 0.44 to 0.25, and then increased to 0.34 with the increase of cooling rate due to the promoted dissolution of Fe^{3+} compounds in aggressive environments. The content of Cr in different valence states changed significantly with the increase of cooling rate. The content of Cr_2O_3 increased first and then decreased, resulting in the increase of $\text{Cr}_{\text{ox}}/\text{Cr}_{\text{hy}}$ ratio from 0.46 at $6 \text{ }^\circ\text{C min}^{-1}$ to 1.21 at $100 \text{ }^\circ\text{C min}^{-1}$. Then it decreases, indicating that at lower or higher cooling rate,

the hydroxide is enriched on the surface of the film, thereby reducing the corrosion resistance (Fig. 8b). The Mo spectra exhibit a doublet due to the low spin–orbit splitting between Mo $3d_{5/2}$ and Mo $3d_{3/2}$ core levels (Fig. 8c). Mo(VI) compounds are the dominant Mo oxidized species, which is beneficial for the passivation of the stainless steels. Ni is more difficult to be oxidized than Fe and Cr, so the role of Ni in the passivation layer is mainly metal form. The surface layer of the passive film is mainly composed of Fe–Ni oxides and Ni hydroxides. At $100 \text{ }^\circ\text{C min}^{-1}$, there are more Ni oxide and hydroxide (Fig. 8d). With the increase of cooling rate, the $\text{O}^{2-}/\text{OH}^-$ ratio increases from 0.17 to 0.69 and then decreases to 0.63 (Fig. 8e), which is consistent with the change of $\text{Cr}_{\text{ox}}/\text{Cr}_{\text{hy}}$.

3.4 Corrosion Morphology Observation

The corrosion morphology of 904L SASS after the electrochemical test is shown in Fig. 9. When the cooling rate is $6 \text{ }^\circ\text{C min}^{-1}$, large and deep corrosion pits appear on the surface of the sample, and these corrosion pits are obviously distributed in the interdendrites. This indicates that the σ precipitation rich in Cr and Mo between the dendrites is the main reason for the decrease in the density of the passive film. With the increase in the cooling rate, the pitting corrosion is obviously weakened, and at the cooling rate of $100 \text{ }^\circ\text{C min}^{-1}$, the surface is smooth, clean, and slightly corroded, and the corrosion pit is obviously the smallest. As the cooling rate continues to increase, the corrosion pits on the surface of the stainless steel sample not only continue to increase, but are also distributed in the interdendrites, and large and deep corrosion pits appear, which is consistent with the distribution of the Cr and Mo contents in the σ phase at different cooling rates. The Cr and Mo contents in the σ phase change with the change in the cooling rate, which makes the matrix near the interdendrites appear to be seriously depleted in Cr and Mo. This increases the defects of the passive film on the surface of the stainless steel, thereby reducing the stability, compactness, and corrosion resistance of the passive film. The sizes of the pitting pits are shown in Fig. 8f. When the cooling rate is $6 \text{ }^\circ\text{C min}^{-1}$, the corrosion pit size is the largest

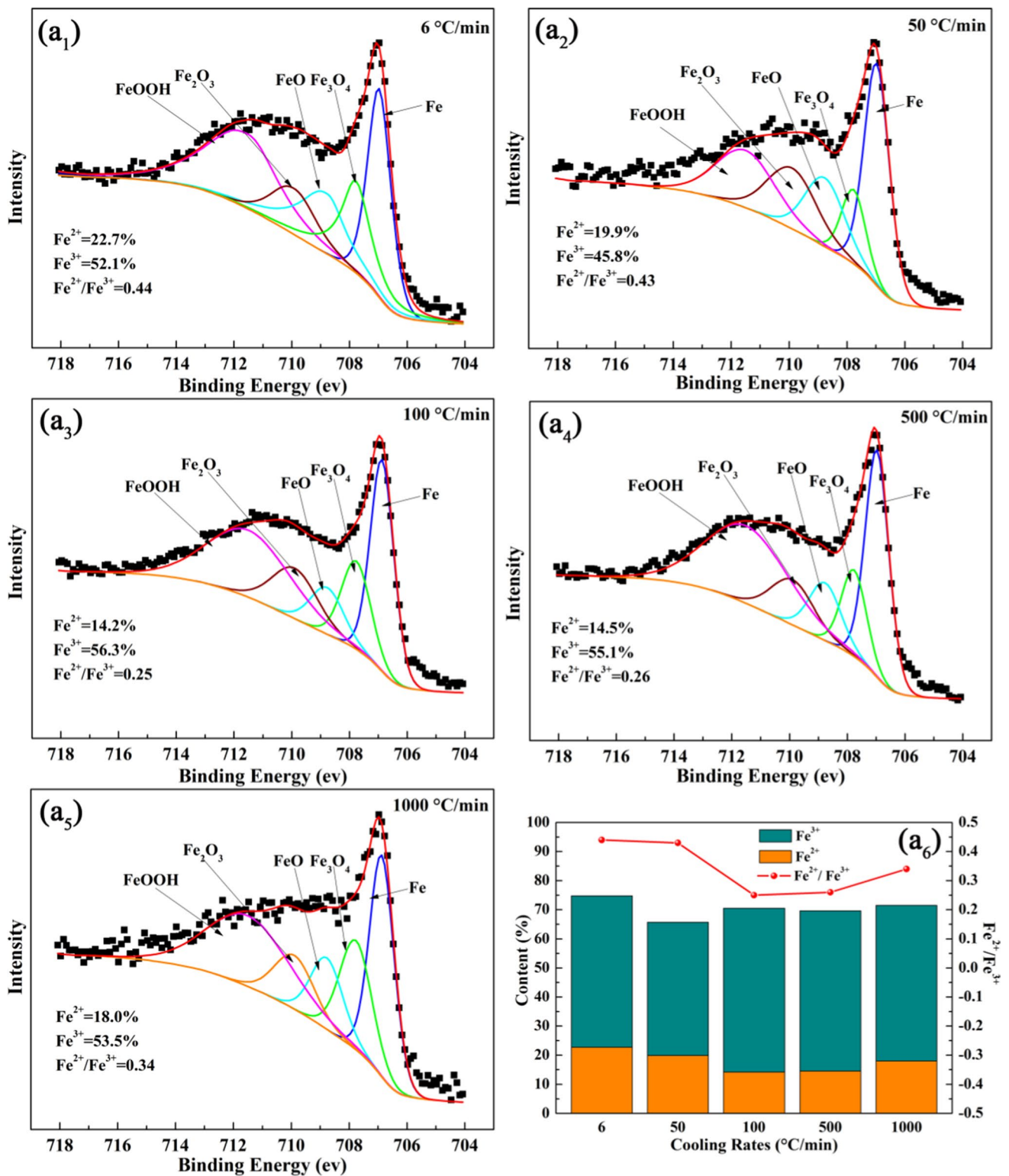


Fig. 8 Detailed XPS spectra of **a** Fe 2p_{3/2}, **b** Cr 2p_{3/2}, **c** Mo 3d, **d** Ni 2p_{3/2}, and **e** O 1 s of the passive film formed on 904L SASS at different cooling rates

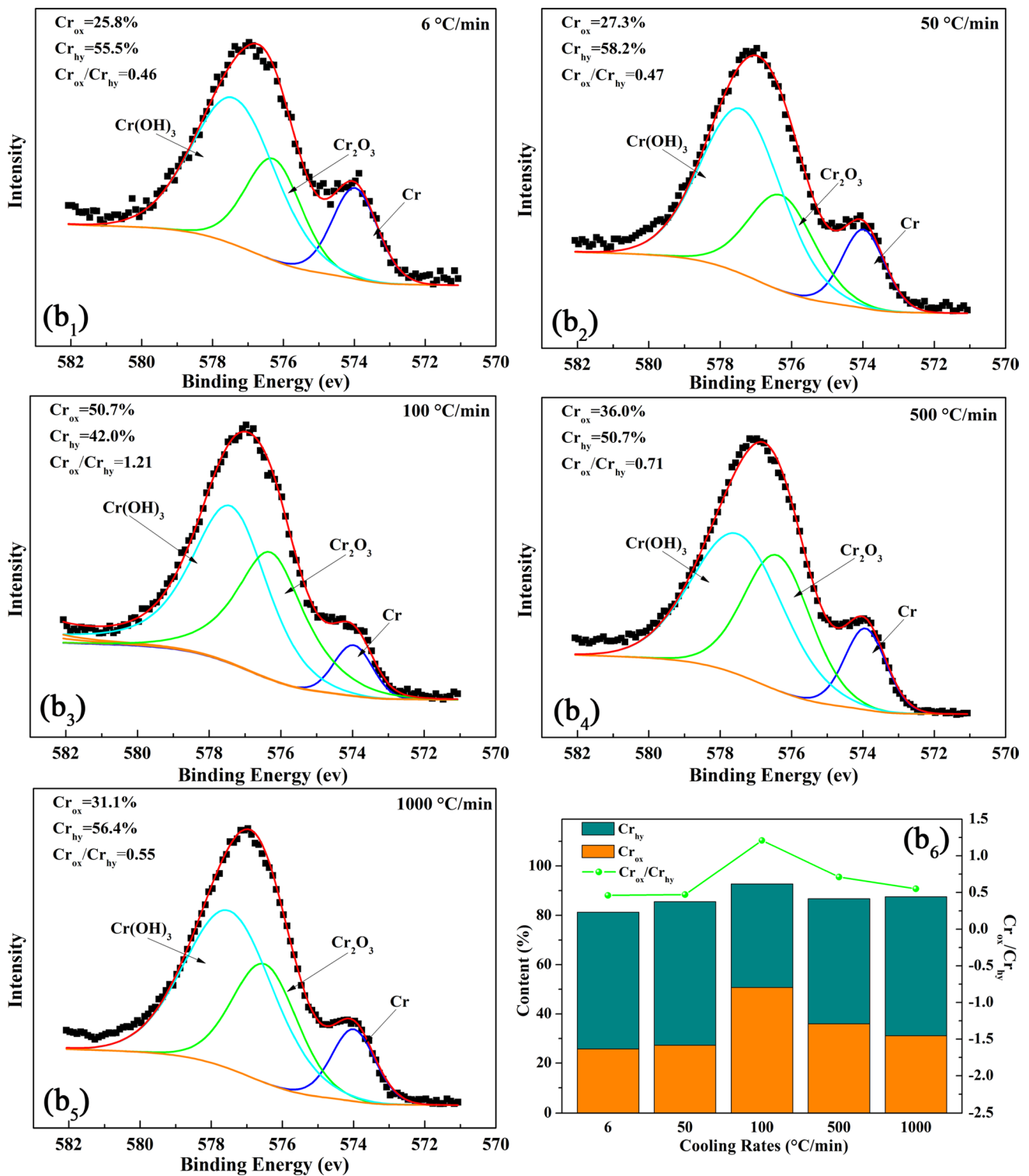


Fig. 8 (continued)

(approximately $78.73 \mu\text{m}$), and when the cooling rate is gradually increased to $100 \text{ }^{\circ}\text{C min}^{-1}$, the corrosion pit size is significantly reduced to $18.18 \mu\text{m}$. When the cooling rate continues to rise to $500 \text{ }^{\circ}\text{C min}^{-1}$, the corrosion

pit size increases to $30.43 \mu\text{m}$, indicating that a high cooling rate has a positive effect on pitting corrosion. When the increase in the cooling rate to $1000 \text{ }^{\circ}\text{C min}^{-1}$, the size of the corrosion pit is $27.65 \mu\text{m}$. Compared with the

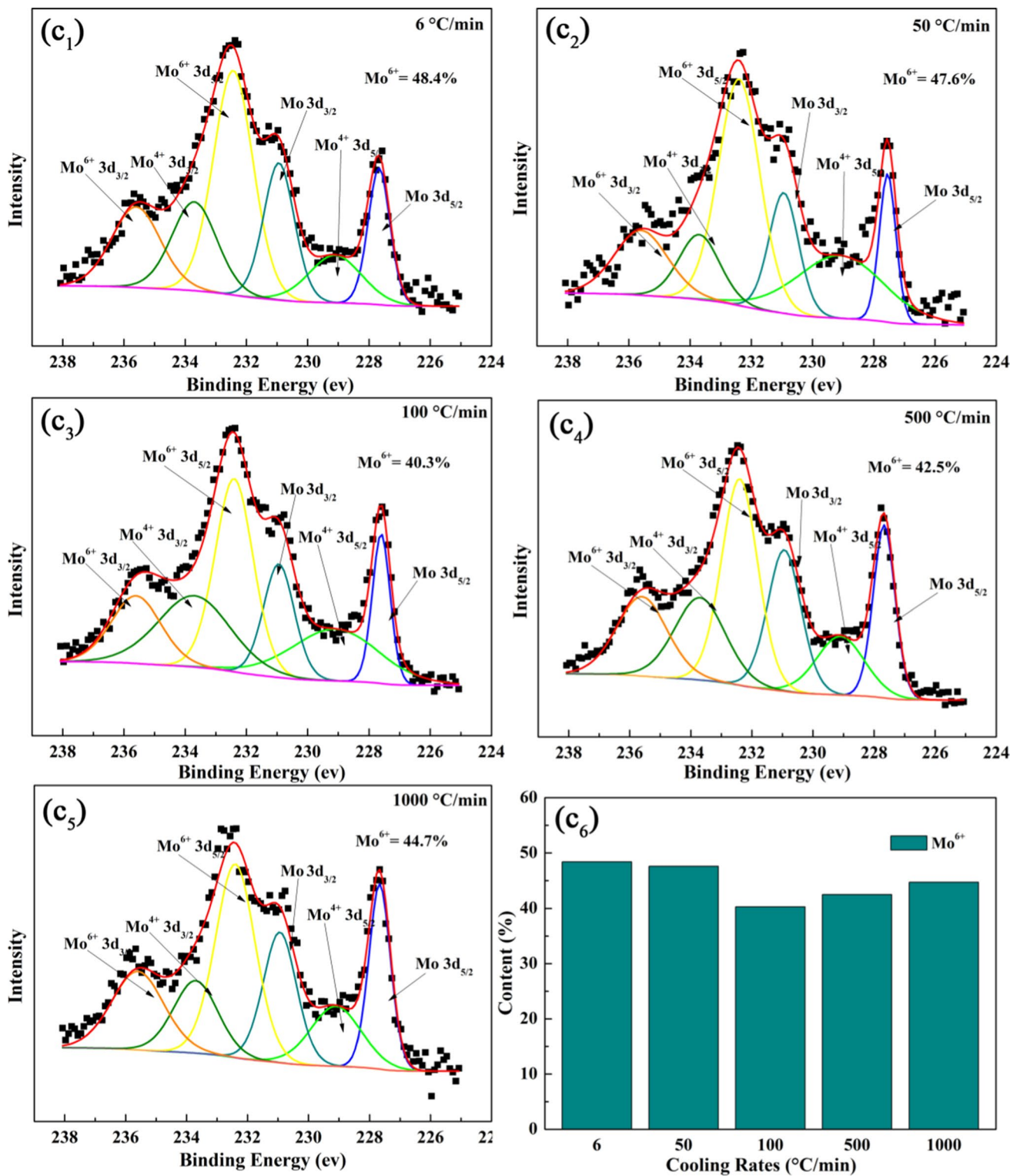


Fig. 8 (continued)

pit size of the 500 °C min⁻¹ (approximately 30.43 μm), although the size is slightly reduced, it is clear that the

depth of corrosion pit increases and the interdendritic corrosion is more serious.

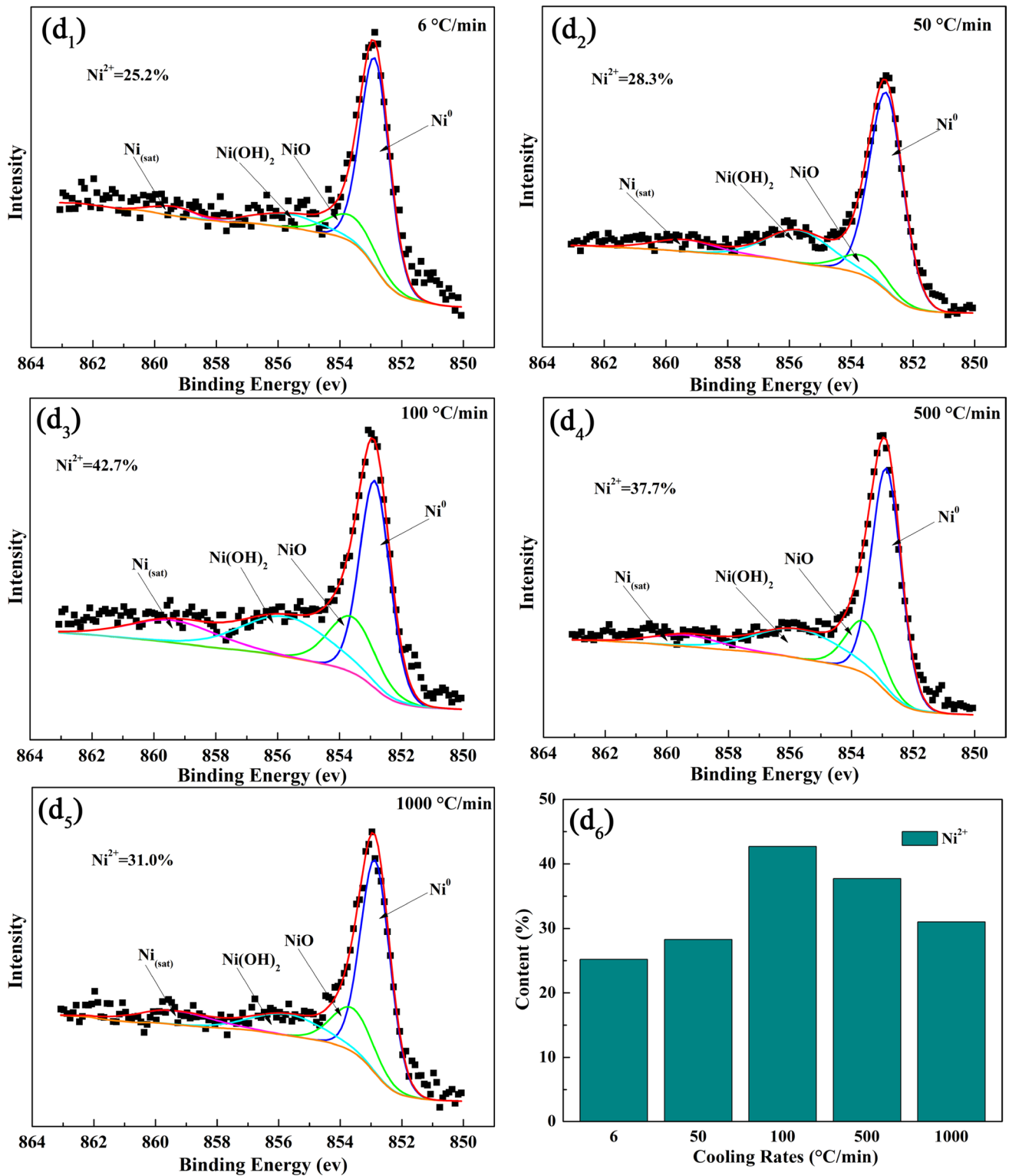


Fig. 8 (continued)

Figure 10 presents the EDS surface scanning analysis after electrochemical corrosion at a cooling rate of 100 °C min⁻¹. Figure 10a shows that the pitting corrosion

pits are mainly distributed around the σ phase. The surface scan spectrum of Fig. 10b–l shows the element distribution around the σ phase. The σ phase is rich in Mo and S,

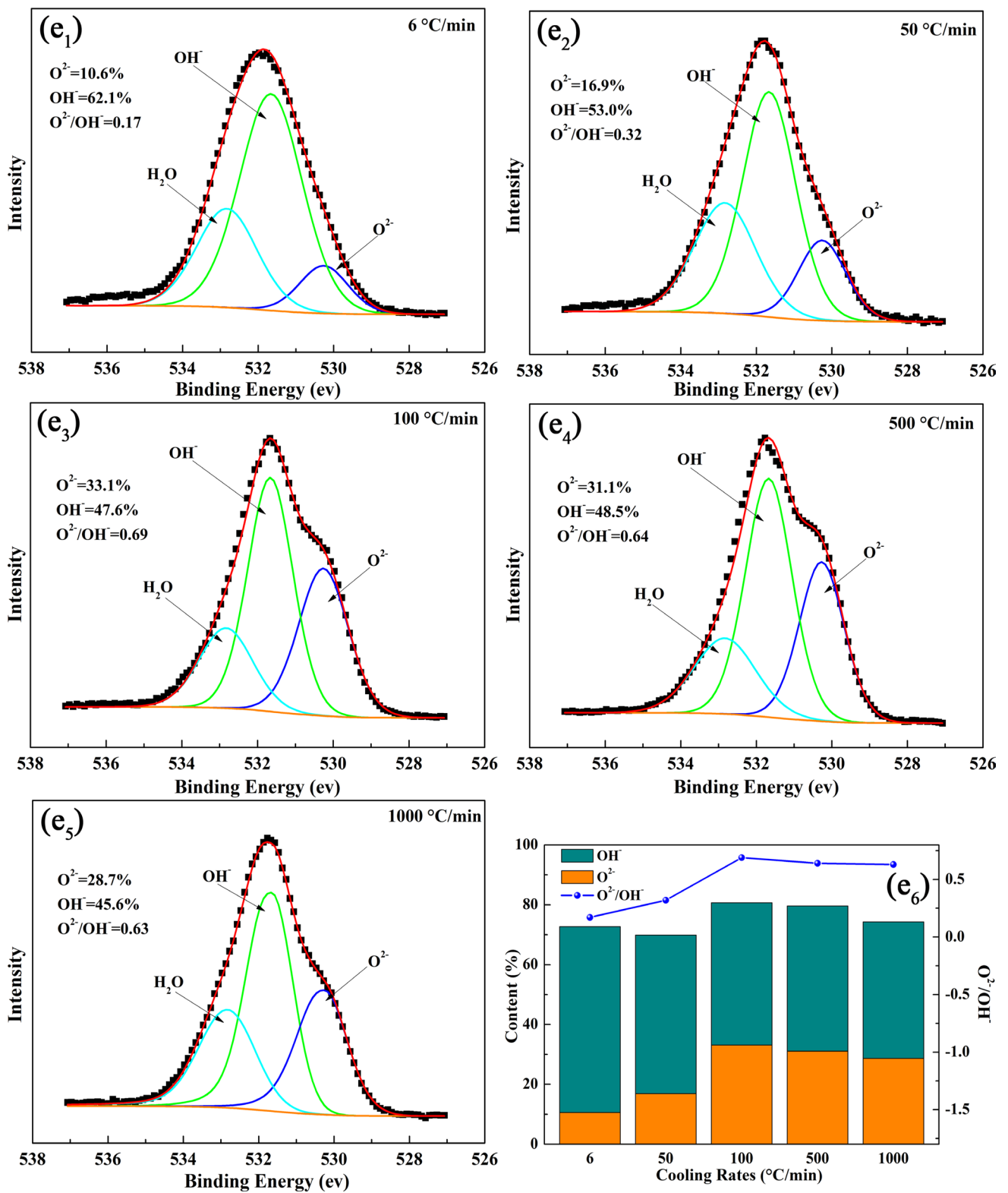


Fig. 8 (continued)

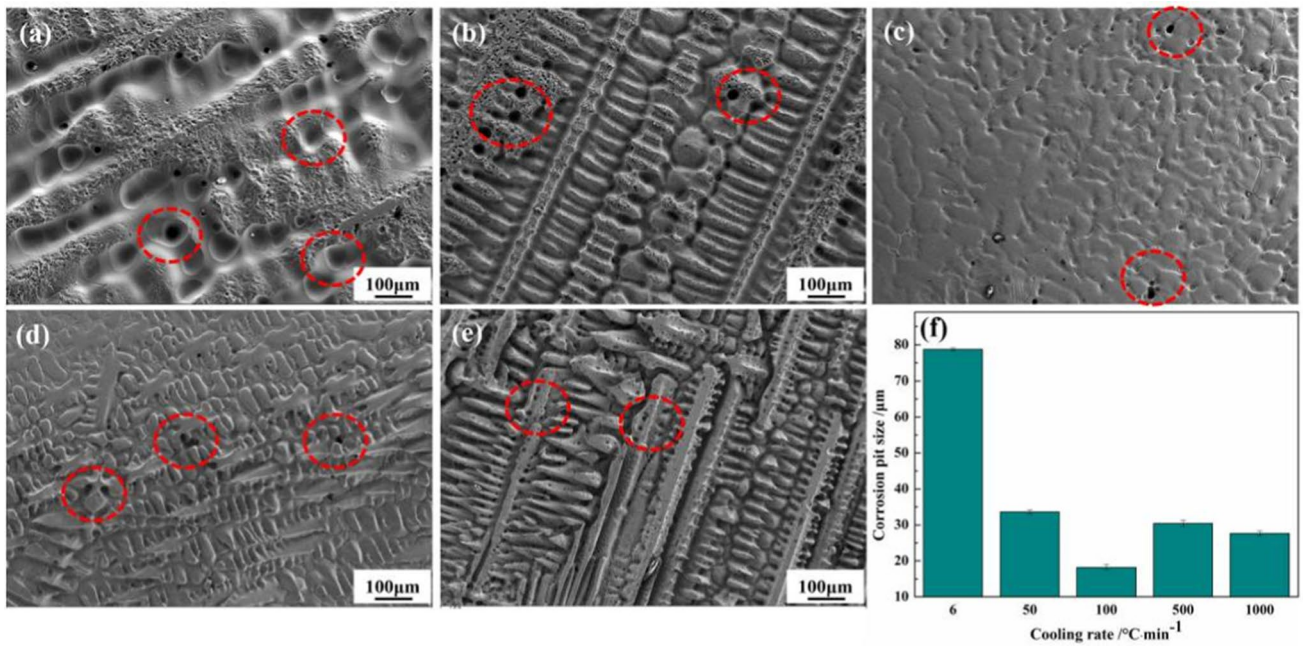


Fig. 9 The 904L SASS corrosion morphology at different cooling rates: **a** 6 °C min⁻¹, **b** 50 °C min⁻¹, **c** 100 °C min⁻¹, **d** 500 °C min⁻¹, **e** 1000 °C min⁻¹, and **f** the size of pitting pits

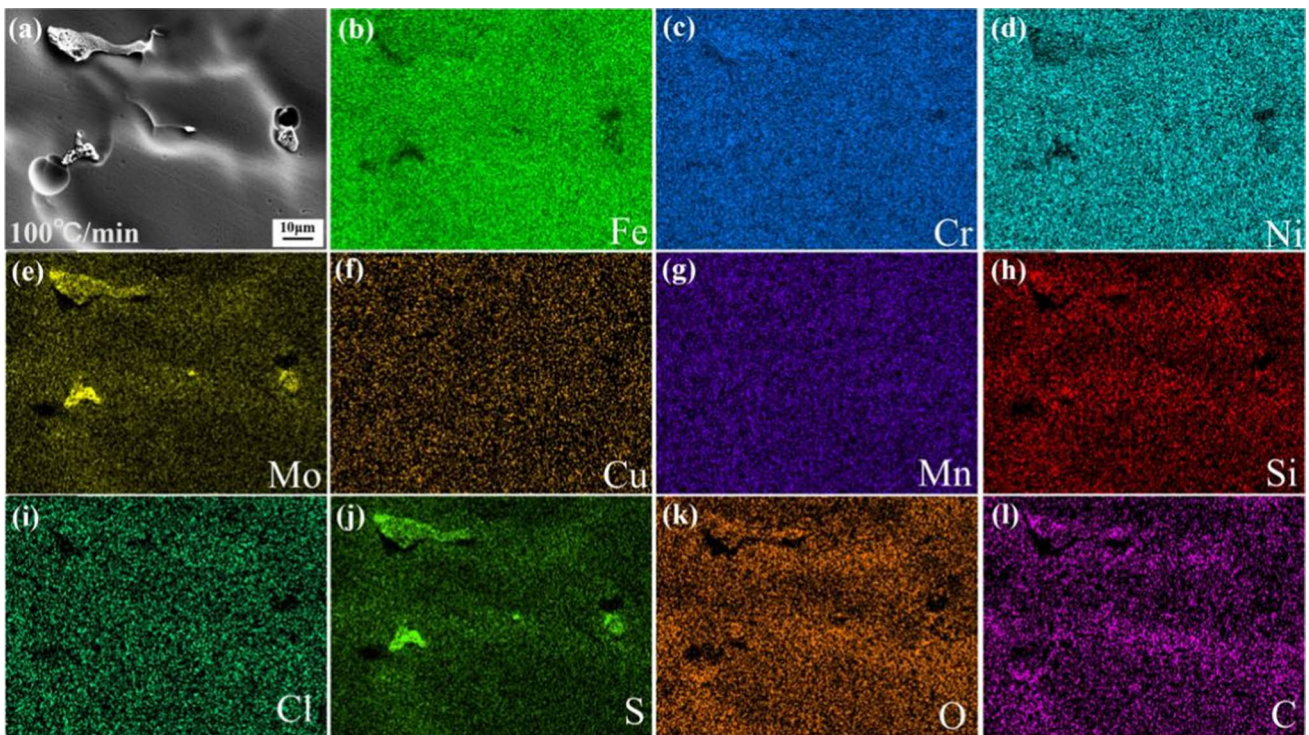


Fig. 10 The EDS element distribution of 904L SASS after electrochemical corrosion at a cooling rate of 100 °C min⁻¹

especially so for Mo; poor in Fe and Ni; slightly rich in Cr, Cl, and O; however, the Cr and Mo contents are poor at the interface between σ phase and austenite matrix. These results show that the Cr and Mo depleted regions are caused by the decrease in the contents of Cr and Mo near the σ phase, which lead to pitting corrosion to occur on the interface between the σ phase and matrix.

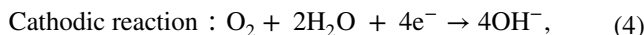
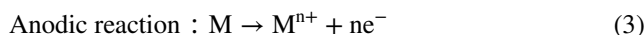
4 Discussion

The corrosion mechanism of 904L SASS at different cooling rates is explained by analyzing the experimental data, as shown in Fig. 11. The difference in corrosion resistance of the 904L SASS is mainly due to the σ phase forming after solidification at different cooling rates. In the 904L A-type solidification mode, the rapid formation of the σ phase is due to the uneven distribution of the elements Cr and Mo. The variation of element segregation and solidification temperature range affects the formation of σ phase during solidification. Moreover, Cr and Mo play an important role in determining the PREN factor. The high precipitation of Cr and Mo in the σ phase leads to a decrease in pitting resistance. With the increase in the cooling rate, the reason for the influence of the solidification process on the σ phase can be explained as follows:

When the cooling rate is $6\text{ }^\circ\text{C min}^{-1}$, the nucleation of γ is slow and the large atoms are excluded from the dendrites, which forms the large flakes and causes the high contents of Cr and Mo in the σ phase. This large σ phase is a defect relative to the matrix, which decreases the uniformity of the stainless

steel microstructure. When the cooling rate is gradually increased to $100\text{ }^\circ\text{C min}^{-1}$, large atoms (Cr and Mo) can be quickly captured at the dendrite trunk position, forming the σ phase with smaller Cr and Mo contents and smaller sizes. The microstructural uniformity of the material is improved, so the uniformity and compactness of the passive film are improved. When the cooling rate continues to increase to $1000\text{ }^\circ\text{C min}^{-1}$, large atoms such as Cr and Mo can be quickly captured at the dendrite trunk position, the nucleation rate of austenite increases rapidly, and the larger-sized atoms cannot diffuse. In a small range of Fe, the Cr and Mo atoms aggregate to the σ phase nucleation conditions, forming an inhomogeneous σ phase in a small range (Fig. 4h, g). Furthermore, the spacing of secondary dendrite decreases with the increase in the cooling rate, resulting in the decrease in the σ nucleation range, which causes the high contents of Cr and Mo in the σ phase to occur at a high cooling rate.

The corrosion resistance of 904L SASS is related to the performance of passive film. In the present work, the pitting corrosion resistance of samples with different Cr and Mo contents in the σ phase is varied. When corrosive ions reach the surface of the steel, the steel begins to dissolve in sufficient oxygen, as described in the reaction below [5]:



where M refers to a metallic element from the steel, including Fe, Cr and Ni. The variable n refers to the valence of

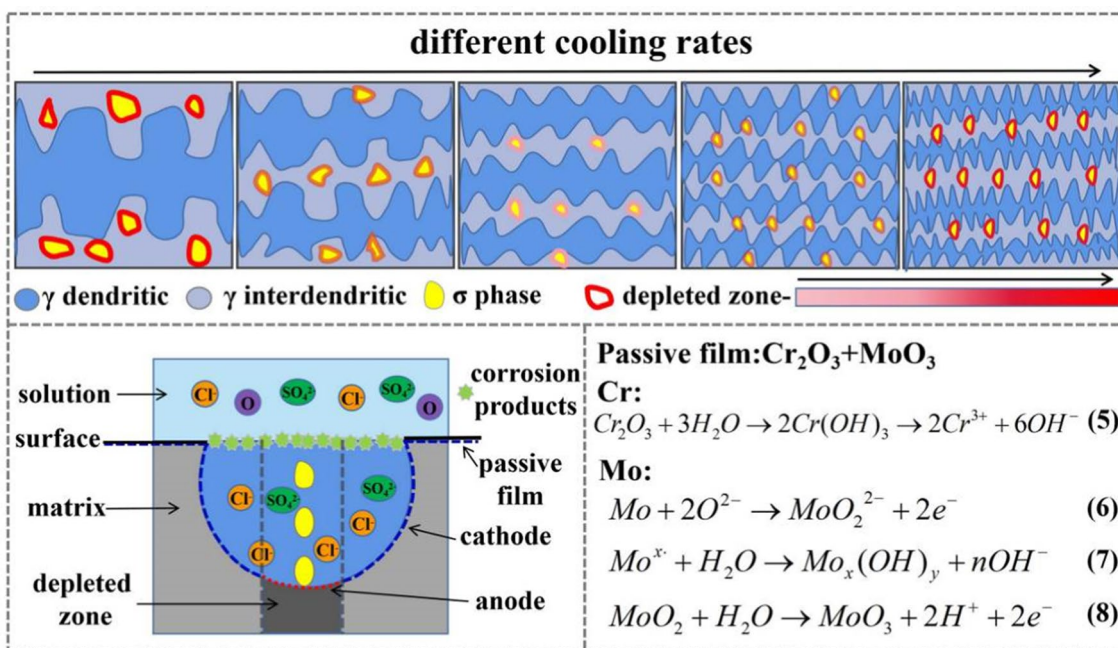


Fig. 11 The corrosion resistance mechanism diagram of 904L SASS at different cooling rates in an FGD solution

M. Hydrolysis reactions of the metal ions occurred to form $M(OH)_n$, but $M(OH)_n$ is unstable and might gradually dehydrate into oxides [40, 41]. Some metal oxides, mainly Cr_2O_3 , form a passive film on the surface of 904L SASS and inhibit iron dissolution and subsequent corrosion. However, stable Cr_2O_3 can be hydrolyzed to $Cr(OH)_3$, and the generated $Cr(OH)_3$ may be hydrolyzed to Cr^{3+} , as shown in formula (5) [42], resulting in poor chromium in the passive film to reduce its corrosion resistance. Molybdenum can be used as an effective barrier to prevent corrosive ions from diffusing through the film, thereby reducing the dissolution rate and anodic current density. Molybdenum also plays a role in the modified active dissolution by forming the insoluble oxides MoO_2 and MoO_3 [as shown in formulas (6)~(8)]. Studies have shown that molybdate is thermodynamically unstable in acidic environments, where only MoO_3 is stable in a strong acidic environment and MoO_2 is stable in a neutral environment [43]. Therefore, the improvement of corrosion resistance is related to the enrichment of Mo on the passive film surface. The corrosion rate can be effectively reduced by generating insoluble molybdenum oxides to prevent the material from passing through the passive film.

However, the σ phase rich in Cr and Mo obviously exists in the steel, which hinders or weakens the formation of the passive film, increases the defects of the passive film, and worsens the compactness, resulting in an increase in the number of corrosion micro-cells and a decrease in the corrosion resistance. The electrode potential of the Mo-rich σ phase is quite different from that of the austenite matrix, and more corrosion micro-cells will be formed. The side with a negative potential becomes an anode and accelerates the dissolution of the passive film. These σ phase / matrix dilution zones constitute the weakest passive film in the corrosion micro-cell area, which can be easily dissolved and ruptured, becoming a favorable position for inducing pitting corrosion. The higher the Mo and Cr content in the σ phase, the more serious the dilution near the dendrites, which increases the pitting tendency of stainless steel and worsens its corrosion resistance.

5 Conclusion

In this study, the effect of the solidification cooling rate on the σ phase precipitation of 904L SASS is studied through microstructure analysis. Electrochemical tests are conducted to study its influence on pitting resistance to determine the corrosion mechanism under different cooling rates. The results are as follows:

- (1) The solidification process of the 904L SASS generally develops into a complete A-type mode, and the solidification temperature and secondary dendrite spacing

decrease with the increase in cooling rate. The surface microstructure of the 904L SASS after solidification shows a γ dendrite and interdendritic precipitation (σ) phase. The σ phase is composed of high Cr and Mo. The contents of Cr and Mo in the σ phase decrease first and then increase with the increase in the cooling rate.

- (2) Electrochemical tests show that it is easy for pitting corrosion to occur due to the existence of the σ phase in steel. Moreover, with the increase in the cooling rate, the pitting corrosion resistance of 904L SASS in the simulated FGD environment shows a law of first increasing and then decreasing. Furthermore, it reached the maximum at $100\text{ }^\circ\text{C min}^{-1}$, indicating that at this cooling rate, the formation of the densest passive film has a good protective effect on the substrate.
- (3) The existence of σ phase leads to the formation of Cr and Mo depletion regions on the σ phase/matrix interface near the interdendritic region, thereby enhancing the coupling effect of the couple. The higher contents of Cr and Mo in the σ phase, the more serious the dilution phenomenon at the interface. Therefore, the cooling rate during solidification should be controlled to delay the formation of the σ phase in 904L SASS to reduce the pitting corrosion in the dilution zone.

Acknowledgements The authors acknowledge support of this work by the National Natural Science Foundation of China (51774226), the Major Program of Science and Technology in Shanxi Province (Nos. 20191102006), the Shaanxi Outstanding Youth Fund project (Grant Number 2021JC-45) and Key international cooperation projects in Shaanxi Province (Grant Number 2020KWZ-007).

Declarations

Conflict of interest We declare that we have no financial and personal relationships with other people or organizations that can inappropriately influence our work, there is no professional or other personal interest of any nature or kind in any product, service and/or company that could be construed as influencing the position presented in, or the review of, the manuscript entitled "Effect of cooling rate on pitting corrosion behavior of 904L austenitic stainless steel in a simulated flue gas desulfurization solution".

References

1. J. Bordzilowski, K. Darowicki, *Anti-Corros. Method. Mater.* **45**, 388 (1998)
2. Z.B. Wang, H.X. Hu, Y.G. Zheng, W. Ke, Y.X. Qiao, *Corros. Sci.* **103**, 50 (2016)
3. Z. Cui, L. Wang, M. Zhong, F. Ge, H. Gao, C. Man, C. Liu, X. Wang, *J. Electrochem. Soc.* **165**, C542 (2018)
4. S. Krakowiak, K. Darowicki, *Prog. Org. Coat.* **117**, 141 (2018)
5. P.Y. Pan, H. Chen, Z.Y. Liang, Q.X. Zhao, *Corros. Sci.* **131**, 126 (2018)
6. Y. Cao, M. Norell, *Oxid. Met.* **80**, 479 (2013)

7. R. Jiang, G. Zou, W. Shi, Y. Liang, S. Xiang, J. Mater. Eng. Perform. **28**, 1863 (2019)
8. I. Betova, M. Bojinov, T. Laitinen, K. Mäkelä, P. Pohjanne, T. Saario, Corros. Sci. **44**, 2675 (2002)
9. B.A.R.S. Barbosa, S.S.M. Tavares, A. Cobuci, M.C.S. de Macêdo, Corrosion **68**, 739 (2012)
10. D. Guo, C.T. Kwok, S.L.I. Chan, L.M. Tam, Surf. Coat. Tech. **408**, 126811 (2021)
11. G.M. Rashed, W.A. Mohrez, A.A.M.A. El-Hamid, I.M. Ghayad, Key Eng. Mater. **835**, 384 (2020)
12. D. Yang, Y.L. Huang, P. Peng, X.J. Liu, B.B. Zhang, Int. J. Electrochem. Sci. **14**, 6133 (2019)
13. G.B. Zou, W. Shi, S. Xiang, J.M. Ji, G.Q. Ma, R.G. Ballinger, RSC Adv. **8**, 2811 (2018)
14. X. Liu, D. Meng, Y. Wang, H. Chen, M. Jin, J. Mater. Eng. Perform. **24**, 1079 (2015)
15. J. Michalska, B. Chmiela, J. Labanowski, W. Simka, J. Mater. Eng. Perform. **23**, 2760 (2014)
16. Y. Han, G.W. Liu, D.N. Zou, R. Liu, G.J. Qiao, Mater. Sci. Eng. A **565**, 342–350 (2013)
17. N. Hiraide, K. Haruhiko, Zairyo-to-Kankyo **58**, 20 (2009)
18. M.J. Perricone, T.D. Anderson, C.V. Robino, J.N. DuPont, J.R. Michael, Metall. Mater. Trans. A **38**, 1976 (2007)
19. M. Torkar, F. Vodopivec, S. Petovar, Mater. Sci. Eng. A **173**, 313 (1993)
20. R.-I. Hsieh, H.-Y. Liou, Y.-T. Pan, J. Mater. Sci. Perform. **10**, 526 (2001)
21. T.H. Chen, J.R. Yang, Mater. Sci. Eng. A **311**, 28 (2001)
22. L.H. Chiu, W.C. Hsieh, C.H. Wu, Mater. Sci. Eng. A **354**, 82 (2003)
23. L. Chen, H. Tan, Z. Wang, J. Li, Y. Jiang, Corros. Sci. **58**, 168 (2012)
24. H. Yan, Z. He, N. Lü, C. Wei, T. Xu, J. Liu, Mater. Corros. **71**, 1257 (2020)
25. J.X. Wang, W. Shi, S. Xiang, R.G. Ballinger, Corros. Sci. **181**, 109234 (2021)
26. M. Benoit, C. Bataillon, B. Gwinner, F. Miserque, M.E. Orazem, C.M. Sánchez-Sánchez, B. Tribollet, V. Vivier, Electrochim. Acta **201**, 340 (2016)
27. C.T. Liu, J.K. Wu, Corros. Sci. **49**, 2198 (2007)
28. A.M.P. Simoes, M.G.S. Ferrira, B. Rondot, M. da Cunha Belo, J. Electrochem. Soc. **137**, 82–87 (1990)
29. J.G. Bai, Y.S. Cui, J. Wang, N. Dong, M.S. Qurashi, H.R. Wei, Y.C. Yang, P.D. Han, J. Iron Steel Res. Int. **26**, 712 (2019)
30. C.S. Wang, Y.S. Wu, Y.A. Guo, J.T. Guo, L.Z. Zhou, J. Alloy. Compd. **784**, 266 (2019)
31. A. Perron, C. Toffolon-Masclat, X. Ledoux, F. Buy, T. Guilbert, S. Urvoy, S. Bossonnet, B. Marini, F. Cortial, G. Texier, C. Harder, V. Vignal, P. Petit, J. Farre, E. Suzon, Acta Mater. **79**, 16 (2014)
32. Y.S. Hao, J. Li, X. Li, W.C. Li, G.M. Cao, C.G. Li, Z.Y. Liu, J. Mater. Process. Tech. **275**, 116326 (2020)
33. A.D. Schino, M.G. Mecozzi, M. Barteri, J.M. Kenny, J. Mater. Sci. **35**, 375 (2000)
34. N. Sato, J. Electrochem. Soc. **129**, 255 (1982)
35. D.E. Williams, M. Fleischmann, J. Stewart, T. Brooks, Mater. Sci. Forum. **8**, 151 (1986)
36. Y. Hou, C. Cheng T. Cao, X. Min, J. Zhao, Int. J. Electrochem. Sci. **13**, 7095 (2018)
37. R.L.D. Monteiro, S.D. Ananda, Rev. Technol. ESPOL **30**, 79 (2017)
38. M.H. Moayed, R.C. Newman, Corros. Sci. **48**, 3513 (2006)
39. C.F. Dong, A.Q. Fu, X.G. Li, Y.F. Cheng, Electrochim. Acta **54**, 628 (2008)
40. Y. Tsutsumi, A. Nishikata, T. Tsuru, Corros. Sci. **49**, 1394 (2007)
41. M.V. Cardoso, S.T. Amaral, E.M.A. Martini, Corros. Sci. **50**, 2429 (2008)
42. S.Y. Kim, H.S. Kwon, H.S. Kim, Solid State Phenomen. **124–126**, 1533 (2007)
43. K.L. Chao, H.Y. Liao, J.J. Shyue, S.S. Lian, Metall. Mater. Trans. B **45**, 381 (2014)

Publisher's Note Springer Nature remains neutral with regard to jurisdictional claims in published maps and institutional affiliations.